J. Fluid Mech. (1995), *vol.* 297, *pp.* 77–100

Fundamental and subharmonic secondary instabilities of Görtler vortices

By FEI LI AND MUJEEB R. MALIK
High Technology Corporation, PO Box 7262, Hampton, VA 23666, USA

(Received 6 December 1993 and in revised form 28 March 1995)

The nonlinear development of stationary Görtler vortices leads to a highly distorted mean flow field where the streamwise velocity depends strongly not only on the wall-normal but also on the spanwise coordinates. In this paper, the inviscid instability of this flow field is analysed by solving the two-dimensional eigenvalue problem associated with the governing partial differential equation. It is found that the flow field is subject to the fundamental odd and even (with respect to the Görtler vortex) unstable modes. The odd mode, which was also found by Hall & Horseman (1991), is initially more unstable. However, there exists an even mode which has higher growth rate further downstream. It is shown that the relative significance of these two modes depends upon the Görtler vortex wavelength such that the even mode is stronger for large wavelengths while the odd mode is stronger for short wavelengths. Our analysis also shows the existence of new subharmonic (both odd and even) modes of secondary instability. The nonlinear development of the fundamental secondary instability modes is studied by solving the (viscous) partial differential equations under a parabolizing approximation. The odd mode leads to the well-known sinuous mode of break down while the even mode leads to the horseshoe-type vortex structure. This helps explain experimental observations that Görtler vortices break down sometimes by sinuous motion and sometimes by developing a horseshoe vortex structure. The details of these break down mechanisms are presented.

1. Introduction

Two-dimensional boundary-layer flow over a concavely curved wall is subject to Görtler instability due to the action of centrifugal force and results in the formation of counter-rotating streamwise vortices. Görtler vortices play a dominant role in boundary-layer transition in many aerodynamic flows such as on turbine blades and supersonic nozzle walls (e.g. Beckwith *et al.* 1984). Owing to their technological importance, Görtler vortices have been the subject of a number of investigations (for recent reviews, see Hall 1990; Floryan 1991; Saric 1994). Görtler vortices are steady and the question of how they might break down to turbulent motion is a problem of fundamental interest in fluid mechanics. In this work, we will study the linear secondary instability characteristics of Görtler vortices and the nonlinear growth of two important modes of secondary instability up to the break down stage.

Experimental investigations have revealed two distinct types of secondary instabilities when the primary instability (the Görtler vortex) is sufficiently developed. Bippes (1978) made detailed observations of Görtler vortex break down using the hydrogen-bubble visualization technique in the Görtler number (G_θ) range of approximately 3 to 9 (based upon momentum thickness θ) where G_θ is defined as

$$G_\theta = R_\theta(\theta|\kappa^\dagger|)^{1/2}, \tag{1.1}$$

$\kappa^{\dagger}$ being the surface curvature and R_θ the Reynolds number based upon momentum thickness. Bippes found that the initial amplification of the Görtler vortices agreed with linear theory and, later, sinuous oscillations developed, which ultimately led to turbulence. Aihara & Koyama (1981) conducted flow visualization studies as well as hot-wire measurements of Görtler vortices in the G_θ range between 7.7 and 15. They found that a different type of secondary instability, i.e. the horseshoe vortex type (also called the varicose instability), was responsible for transition. Ito (1985) also found this symmetric mode of break down in his experiment conducted for G_θ between 5.5 and 12.4. Swearingen & Blackwelder (1987, referred to as SB hereafter) studied Görtler vortices using smoke-wire and hot-wire techniques for G_θ between 0.5 and 10. They observed that both the sinuous and the horseshoe types of secondary instabilities were present in the transition process and found that the sinuous mode was the stronger of the two. In their experiment, the unsteady secondary instability fluctuations correlated better with the spanwise velocity gradients than with the normal velocity gradient. Unsteady motion in Görtler vortices was also observed by Peerhossaini & Wesfried (1988).

Numerical simulations have been carried out by a number of researchers (e.g. Sabry & Liu 1991; Hall 1990; Lee & Liu 1992; Malik & Li 1993) for nonlinear Görtler vortices under the same conditions as the experiment of SB. Agreement with the experiment was obtained for the early stages of Görtler vortex development. More recently, Guo & Finlay (1994) studied spatially developing nonlinear Dean and Görtler vortices and explained the wavenumber selection mechanism and the irregularities associated with vortex structures found in the experiments. Unsteady oscillations in Görtler vortices have been studied by Hall & Horseman (1991) and Yu & Liu (1991, 1994). Hall & Horseman (1991) derived a partial differential equation governing the inviscid secondary instability for a mean flow which varied strongly in two directions. They identified the two-dimensional odd and even eigenfunctions of this equation as respectively representing the sinuous and varicose types of secondary instability of the Görtler vortex. They also found that the odd mode grows faster than the even mode. The same conclusion was reached by Yu & Liu (1991, 1994) who performed viscous calculations. In the temporal simulation of Liu & Domaradzki (1993), the sinuous mode was also found to be stronger than the varicose mode.

All these numerical investigations of secondary instability seem to point to one fact: the sinuous mode is the dominant mode and is chiefly responsible for the transition to turbulence. Why do then some experiments (e.g. Aihara & Koyama 1981) show the presence of only the varicose mode? Examining the above-cited numerical results closely, we find that most of these calculations were carried out for either a limited range of wavelengths or a limited number of streamwise locations. In Hall & Horseman (1991), for example, the secondary instability calculations were computed almost exclusively at $x = 100$ cm. In Liu & Domaradzki (1993), the computational box had streamwise dimension of either 2 or 2.2 cm, which essentially fixed the streamwise wavelength.

In this paper, we perform a more comprehensive study and analyse various modes of secondary instability and the effect of Görtler vortex wavelength on the relative importance of odd and even modes. Previous studies have addressed only the fundamental mode (i.e. spanwise wavelength equal to the Görtler vortex wavelength) of instability. However, we will investigate both fundamental and subharmonic modes. We also study the nonlinear evolution of the secondary instability modes using parabolized stability equations (PSE) (see Herbert 1991; Bertolotti, Herbert & Spalart 1992; Chang *et al.* 1991). Section 2 formulates the parabolized stability equation which

describes all stages of the vortex development. Section 3 deals with linear secondary instability while §4 addresses the nonlinear evolution of secondary instabilities. Conclusions are drawn in §5.

2. Problem formulation for nonlinear steady and unsteady disturbances

We consider a two-dimensional zero-pressure-gradient boundary-layer flow over a concave surface whose constant radius of curvature $r^\dagger = 1/\kappa^\dagger$. The streamwise, wall-normal and spanwise coordinates are denoted as $x = X/l_0$, $y = Y/l_0$ and $z = Z/l_0$, respectively ($y = 0$ denotes the wall), where the lengthscale l_0 will be prescribed later.

Let the x-, y- and z-components of the velocity and pressure be given by

$$(u^\dagger, v^\dagger, w^\dagger) = U_e\{U(x,y)+u(x,y,z,t), V(x,y)+v(x,y,z,t), 0+w(x,y,z,t)\},$$
$$p^\dagger = \rho U_e^2(P+p(x,y,z,t)),$$

where the superscript $\dagger$ represents a dimensional quality and U_e is the velocity scale. Here U and V are mean-flow velocity components obtained by solving the Blasius equation whereas u, v, w represent the perturbation velocity components in the x-, y-, z-directions, respectively. Similarly, P and p represent the mean and perturbation pressures. We assume that Reynolds number, R, is large and that the radius of curvature is much larger than the boundary-layer thickness, δ (i.e. $k^\dagger\delta \ll 1$). In this case, if $\kappa = \kappa^\dagger l_0$, the equations governing the perturbations quantities are

$$\frac{\partial u}{\partial t}+U\frac{\partial u}{\partial x}+u\frac{\partial U}{\partial x}+V\frac{\partial u}{\partial y}+v\frac{\partial U}{\partial y}+\kappa(Uv+Vu)+\frac{\partial p}{\partial x}-\frac{1}{R}\nabla^2 u = N_1, \tag{2.1}$$

$$\frac{\partial u}{\partial t}+U\frac{\partial v}{\partial x}+u\frac{\partial V}{\partial x}+V\frac{\partial v}{\partial y}+v\frac{\partial V}{\partial y}-2\kappa Uu+\frac{\partial p}{\partial y}-\frac{1}{R}\nabla^2 v = N_2, \tag{2.2}$$

$$\frac{\partial w}{\partial t}+U\frac{\partial w}{\partial x}+V\frac{\partial w}{\partial y}+\frac{\partial p}{\partial y}-\frac{1}{R}\nabla^2 w = N_3, \tag{2.3}$$

$$\frac{\partial u}{\partial x}+\frac{\partial v}{\partial y}+\frac{\partial w}{\partial z}+\kappa v = 0, \tag{2.4}$$

where N_1, N_2 and N_3 represent the nonlinear terms

$$N_1 = -u\frac{\partial u}{\partial x}-v\frac{\partial u}{\partial y}-w\frac{\partial u}{\partial z}-\kappa uv, \quad N_2 = -u\frac{\partial u}{\partial x}-v\frac{\partial v}{\partial y}-w\frac{\partial v}{\partial z}+\kappa u^2,$$

$$N_3 = -u\frac{\partial w}{\partial x}-v\frac{\partial w}{\partial y}-w\frac{\partial w}{\partial z},$$

and

$$\nabla^2 = \frac{\partial^2}{\partial x^2}+\frac{\partial^2}{\partial y^2}+\frac{\partial^2}{\partial z^2}+\kappa\frac{\partial}{\partial y}.$$

The boundary conditions are

$$u = v = w = 0 \quad \text{at} \quad y = 0 \quad \text{and} \quad u \to 0, \quad v \to V_m(x), \quad w \to 0 \quad \text{as} \quad y \to \infty,$$

where V_m signifies a non-zero value. Periodic boundary conditions are imposed in the spanwise direction. Here, l_0 and U_e are constants so as to defined Reynolds number R as

$$R = U_e l_0/\nu,$$

where the lengthscale $l_0 = (\nu X_0/U_e)^{1/2}$, X_0 being the location (dimensional) of a reference streamwise station, and ν the kinematic viscosity. Another important parameter which is a measure of the wall curvature is the Görtler number G defined as $G = R|\kappa|^{1/2}$. The reason why v does not go to zero outside the boundary layer is that the vertical velocity perturbation vanishes for all Fourier modes (see (2.5) below) except the mean-flow correction mode.

We use the method of parabolized stability equations (PSE) for our computations. Here, we follow the formulation of Malik & Li (1992) (see also Malik, Li & Chang 1994) and let $\boldsymbol{\phi} = (u, v, w, p)$ be the disturbance vector and assume that the disturbance takes the form

$$\boldsymbol{\phi} = \sum_m \sum_n \hat{\boldsymbol{\phi}}_{mn}(x, y) \exp\left\{ \mathrm{i} \int_{x_0}^{x} \alpha_{mn}(\xi)\, \mathrm{d}\xi + \mathrm{i} n \beta z - \mathrm{i} m \omega t \right\}, \tag{2.5}$$

where α_{mn} and β are the x and z wavenumbers, ω is the perturbation frequency and $\hat{\boldsymbol{\phi}}_{mn}$ is the amplitude function for the mode $(m\omega, n\beta)$. Substituting (2.5) into (2.1)–(2.4), we obtain a set of equations with $\hat{\boldsymbol{\phi}}_{mn}$ and α_{mn} as unknowns. Since, there are now more unknowns (namely, α_{mn}) than equations, another condition is needed for the closure of the system. Since the basic flow is slowly varying in the streamwise direction, a condition on $\hat{\boldsymbol{\phi}}_{mn}$ is imposed such that most of the waviness and growth of the perturbation is absorbed into the exponential function in (2.5), making the amplitude function $\hat{\boldsymbol{\phi}}_{mn}$ slowly varying with respect to x. The terms containing $\partial^2 \hat{\boldsymbol{\phi}}_{mn}/\partial x^2$ can thus be dropped and the only second derivatives left in the governing equations are those with respect to y. These new stability equations are parabolized in the sense of the parabolized Navier–Stokes (PNS) equation for mean-flow computations. The condition for choosing α_{mn} and minimizing the streamwise variation of the amplitude function can take several forms. In the present work, we choose α_{mn} to be such that the following integral vanishes:

$$\int_0^\infty (\hat{u}^*, \hat{v}^*, \hat{w}^*) \frac{\partial}{\partial x} \begin{pmatrix} \hat{u} \\ \hat{v} \\ \hat{w} \end{pmatrix} \mathrm{d}y = 0, \tag{2.6}$$

where * denotes the complex conjugate. The PSE can be written in matrix form as

$$\boldsymbol{L}_0 \hat{\boldsymbol{\phi}}_{mn} + \boldsymbol{L}_1 \frac{\partial \hat{\boldsymbol{\phi}}_{mn}}{\partial y} + \boldsymbol{L}_2 \frac{\partial^2 \hat{\boldsymbol{\phi}}_{mn}}{\partial y^2} + \boldsymbol{L}_3 \frac{\partial \hat{\boldsymbol{\phi}}_{mn}}{\partial x} = \boldsymbol{N}_{mn}, \tag{2.7}$$

$$F(\hat{\boldsymbol{\phi}}_{mn}, \alpha_{mn}) = 0, \tag{2.8}$$

where the coefficient matrices contain the Blasius flow quantities as well as α_{mn}, β and ω. Equation (2.8) is a general form of (2.6). The matrix operators $\boldsymbol{L}_0$–$\boldsymbol{L}_3$ and N_{mn} are given in the Appendix. The boundary conditions are

$$\hat{u}_{mn} = \hat{v}_{mn} = \hat{w}_{mn} = 0 \quad \text{at} \quad y = 0, \tag{2.9a}$$

$$\hat{u}_{mn}, \hat{v}_{mn} (\text{except for } m = n = 0), \hat{w}_{mn} \to 0 \quad \text{as} \quad y \to \infty. \tag{2.9b}$$

No boundary condition is required for $\hat{v}(\infty)$ when $m = n = 0$.

We discretize the PSE using discrete Fourier transforms in the spanwise direction and in time. In the direction normal to the wall, we use the fourth-order compact difference scheme (Malik, Chuang & Hussaini 1982) which requires that (2.7) be written as a system of first-order equations. Numerical computation starts at some streamwise location x_0 where the velocity components are prescribed for a given

wavenumber α_{mn}; the velocities and pressure at $x_0 + \mathrm{d}x$ are calculated using backward Euler discretization. If (2.8) were not satisfied, a new α_{mn} would be chosen and the equations solved again. This iterative process continues until (2.8) is satisfied, and the computation proceeds to the next streamwise location. During this iterative process, nonlinear terms are also updated and one makes sure that they are converged before the solution proceeds downstream. We note that the PSE approximation is only valid for convective instabilities. If the flow were to be subject to absolute instabilities (Huerre & Monkewitz 1990), the approximation would break down.

3. Linear inviscid secondary instability

3.1. *Basic flow*

In order to obtain the three-dimensional basic flow for linear stability analysis, we first solve the steady form ($\omega = 0$) of the governing partial differential equations given in §2 above. In the limit $R \to \infty$, and $\kappa \to 0$ with G held fixed, and by rescaling the dependent and independent variables ($V = O(1/R)\,U, (v, w) = O(1/R)\,u, (y, z) = O(1/R)\,x$) the parabolic equations derived by Hall (1983, 1988) can be recovered from (2.1)–(2.4). In Hall (1988) a further step is taken to eliminate the spanwise velocity and the pressure from the linear terms in (2.7), resulting in a coupled system of fourth-order and second-order equations. However, we will solve (2.7) directly in the primitive $(\hat{u}, \hat{v}, \hat{w}, \hat{p})$ formulation, except that the condition imposed on α, (2.8), is not applied since α is identically 0.

The flow parameters used in the present analysis are taken from the experiment of SB. The radius of curvature of the concave surface is 320 cm and free-stream velocity is 500 cm s^{-1}. The streamwise range of interest in our analysis lies approximately $10 < X < 120$ cm, in which the Reynolds number based on the distance from the leading edge ($Re = R^2$) ranges from 3.3×10^4 to 4×10^5 and the Görtler number G_θ ranges from 1.3 to 8.3. Calculations are started at $X = 10$ cm with initial amplitude $u = 0.0187 U_e$ estimated from the experimental data of SB for disturbances of wavelengths $\lambda_z = 0.9$, 1.8 and 3.6 cm. The number of spanwise Fourier modes used in the z-direction is 11 (i.e. n goes from -10 to 10 in (2.5)), and the streamwise marching step size is 0.821 58 cm. Therefore, approximately 130 marching steps are taken in the streamwise direction. The number of wall-normal steps is 121. The free-stream boundary conditions are imposed at a height of about 20 boundary-layer thicknesses. This is sufficient since the perturbations decay exponentially with y. The solution was tested by changing the number of grid points and it was found to be grid-independent.

The energy in each Fourier mode is shown in figures 1(*a*) and 1(*b*) for $\lambda_z = 0.9$, and 3.6 cm, respectively. Here, energy is defined as

$$E_n = \int_0^\infty (|\hat{u}_n|^2 + |\hat{v}_n|^2 + |\hat{w}_n|^2)\,\mathrm{d}y; \quad n > 0 \tag{3.1a}$$

and

$$E_0 = \frac{1}{2}\int_0^\infty (|\hat{u}_0|^2 + |\hat{w}_0|^2)\,\mathrm{d}y. \tag{3.1b}$$

The omission of the velocity component normal to the wall $\hat{v}_0$, from (3.1*b*) is necessary because $\hat{v}_0$ does not vanish as $y \to \infty$. The integral in (3.1*b*) would not exist if $\hat{v}_0$ were included.

Initially, the Görtler vortex (mode 1) develops approximately linearly, but later on it begins to saturate (compare with the linear result). Owing to nonlinearity, higher harmonics (modes 2, 3, ...) and a mean-flow correction mode (mode 0) are generated.

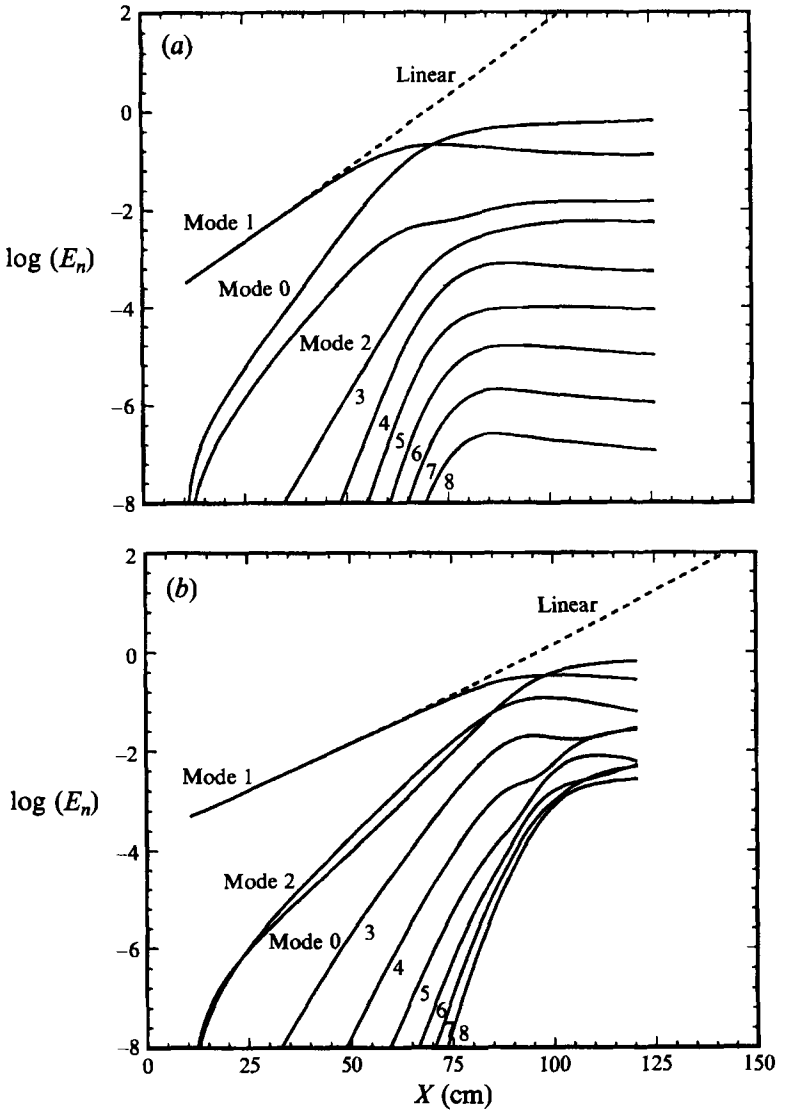

FIGURE 1. Nonlinear evolution of disturbance energy for various spanwise Fourier modes: (*a*) $\lambda_z = 0.9$ cm, (*b*) $\lambda_z = 3.6$ cm.

For the low-wavelength case ($\lambda_z = 0.9$ cm), mode 0 is dominant over mode 2 right from the beginning. At $x \approx 72$ cm, mode 0 overtakes even the fundamental mode (mode 1). Thus in this nonlinear regime, the basic interaction is between the fundamental and the mean-flow correction (mode 0). The dominance of the mean-flow correction mode in figure 1(*a*) is consistent with the results obtained by Hall & Lakin (1988) using the small-wavelength asymptotic analysis. For the longer-wavelength case, the energy in modes 0 and 2 is comparable up to $x \approx 80$ cm and it is only after $x \approx 100$ cm that mode 0 overtakes mode 1. The results in figure 1(*b*), therefore, suggest that for long-wavelength nonlinear Görtler vortices, both mode 0 and mode 2 are important in the nonlinear evolution.

The experiment of SB (as well as others) produced 'mushroom-like' structures for the streamwise velocity due to the pumping action of the counter-rotating vortices. Our

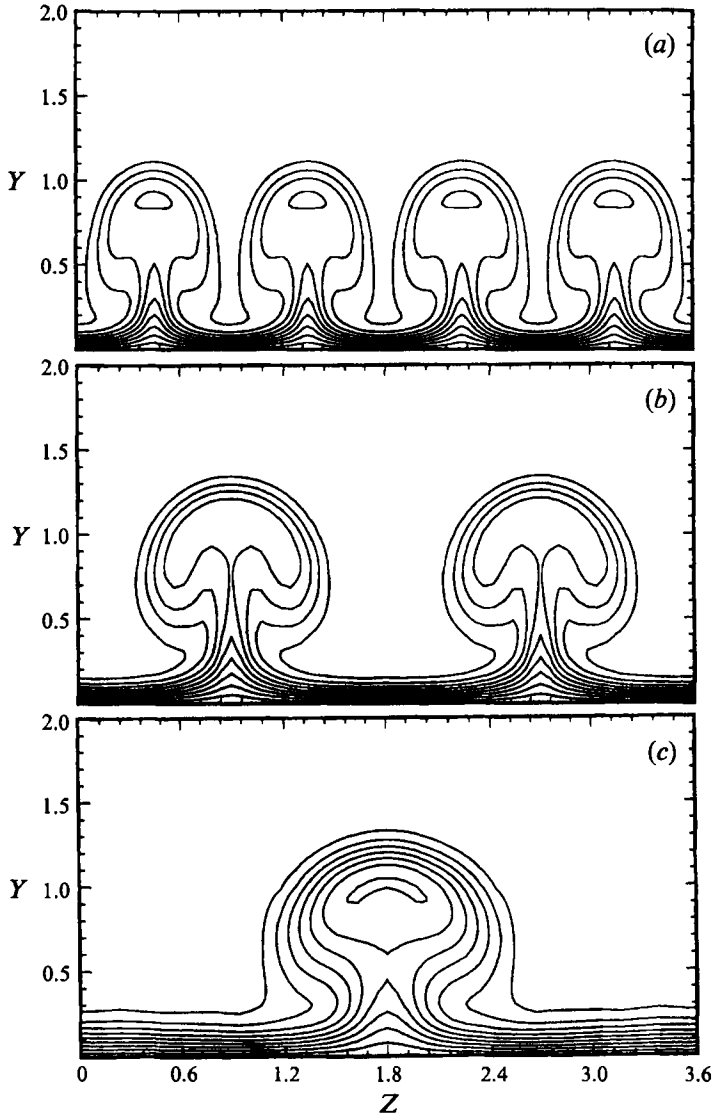

FIGURE 2. Variation of streamwise velocity in the (Y, Z)-plane due to the presence of Görtler vortices at $X = 100$ cm: (*a*) $\lambda_z = 0.9$ cm, (*b*) $\lambda_z = 1.8$ cm, (*c*) $\lambda_z = 3.6$ cm. Contours range from $u/u_e = 0.1$ to 0.9 in increments of 0.1.

computed structures for $\lambda_z = 1.8$ cm are similar to those given by Lee & Liu (1992). In the early stages of the development, the amplitude of the u-perturbation is small and the velocity contours show a wavy spanwise structure. As the Görtler vortices gather strength at relatively large distances downstream the same 'mushroom' structures as observed in the experiment of SB are recovered. The regions in the neighbourhood of the centrelines of the mushrooms are referred to as 'peak' regions where the streamwise velocity is relatively low; and the regions between the mushrooms are referred to as 'valley' regions where the streamwise velocity is relatively high. These mushrooms at $x = 100$ cm are shown for $\lambda_z = 0.9$, 1.8 and 3.6 cm in figure 2. Clearly, the valley region becomes much wider as the wavelength increases. We will see later

that the relative significance of secondary instability modes depends upon Görtler vortex wavelengths. The streamwise velocity profiles in the peak plane become wake-like and it will be shown below that the high-shear-layer region up in the peak plane will become subject to a particular mode of secondary instability. Similarly, the spanwise distribution of the streamwise velocity component is also inflectional and becomes subject to another mode of secondary instability, as also found by Hall & Horseman (1991) and Yu & Liu (1991).

We will use the steady Görtler vortex flow field generated above as the basic flow state for our secondary instability analysis given in the next subsection. Thus, if u_G, v_G, w_G are the perturbation velocities due to the Görtler vortex, the new mean flow whose stability will be analysed in the next subsection is

$$\bar{u} = U+u_G, \quad \bar{v} = V+v_G, \quad \bar{w} = W+w_G.$$

3.2. *Linear stability equations*

We assume that the streamwise variation of the new mean flow ($\bar{u}$, $\bar{v}$, $\bar{w}$) is small compared with the wavelength of the secondary disturbance. This assumption can be justified *a posteriori* from the results. Therefore, the linear secondary oscillation can be written as

$$\psi(x,y,z,t) = \hat{\psi}(y,z)\,\mathrm{e}^{\mathrm{i}(\alpha x-\omega t)},$$

where $\psi = (u_s, v_s, w_s, p_s)$ and $\hat{\psi} = (\hat{u}_s, \hat{v}_s, \hat{w}_s, \hat{p}_s)$; α is the wavenumber, ω is the oscillation frequency, and the subscript s indicates secondary instability. Here, we consider only the temporal instability; therefore α is real and ω is complex. The flow field is unstable to disturbances if $\omega_i > 0$.

We note that $\bar{v}(y,z)$ and $\bar{w}(y,z)$ are much smaller than $\bar{u}(y,z)$. Then, following Hall & Horseman (1991), the equations governing the linear secondary instability are

$$\mathrm{i}\alpha\hat{u}_s+\frac{\partial\hat{v}_s}{\partial y}+\frac{\partial\hat{w}_s}{\partial z} = 0, \tag{3.3}$$

$$\mathrm{i}\alpha(\bar{u}-c)\,\hat{u}_s+\frac{\partial\bar{u}}{\partial y}\hat{v}_s+\frac{\partial\bar{u}}{\partial z}\hat{w}_s = -\mathrm{i}\alpha\hat{p}_s, \tag{3.4}$$

$$\mathrm{i}\alpha(\bar{u}-c)\,\hat{v}_s = -\frac{\partial\hat{p}_s}{\partial y}, \tag{3.5}$$

$$\mathrm{i}\alpha(\bar{u}-c)\,\hat{w}_s = -\frac{\partial\hat{p}_s}{\partial z}, \tag{3.6}$$

where $c = \omega/\alpha$ is the (complex) disturbance phase velocity. Eliminating $\hat{u}_s$, $\hat{v}_s$, $\hat{w}_s$, we obtain the equation governing the secondary pressure oscillation (after dropping subscript s):

$$\left(\frac{\partial^2}{\partial y^2}+\frac{\partial^2}{\partial z^2}-\alpha^2\right)\hat{p}-\frac{2\bar{u}_y\hat{p}_y}{\bar{u}-c}-\frac{2\bar{u}_z\hat{p}_z}{\bar{u}-c} = 0. \tag{3.7}$$

The boundary conditions are

$$y = 0, \quad \hat{p}_y(y,z) = 0; \qquad y\to\infty, \quad \hat{p}(y,z)\to 0, \tag{3.8a, b}$$

and

$$\hat{p}(y,z) = \hat{p}(y,z+\lambda_z), \tag{3.9a}$$

where λ_z is the Görtler vortex wavelength. Equation (3.9a) yields the fundamental

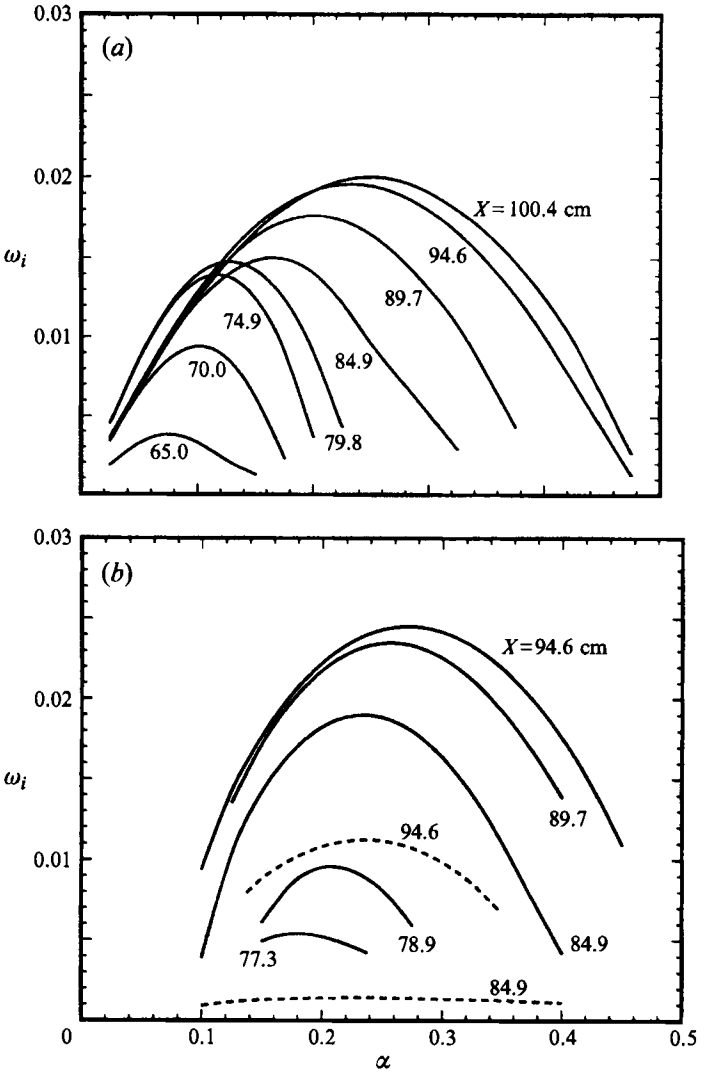

FIGURE 3. Secondary instability temporal growth rate variation with spanwise wavenumber at various streamwise locations. (*a*) Odd mode, (*b*) even mode, the broken line shows the second even mode.

mode of secondary instability. The subharmonic mode can be obtained by replacing (3.9*a*) with

$$\hat{p}(y,z) = p(y,z+2\lambda_z). \tag{3.9b}$$

Equations (3.7)–(3.9) constitute an eigenvalue problem which is solved by using a Chebyshev collocation method in the y-direction and a Fourier collocation method in the z-direction with appropriate grid stretchings in both directions to concentrate more collocation points in regions of high gradients. Furthermore, since the basic flow state is symmetric, the eigenfunctions can be split into families of even and odd modes. For the even mode $\hat{p}(y,z) = \hat{p}(y,-z)$ and for the odd mode $\hat{p}(y,z) = -\hat{p}(y,-z)$. Taking advantage of the symmetry conditions, we reduce the size of the resulting discretized system by approximately half. The discretized system can be represented in the form

$$\boldsymbol{A}\boldsymbol{\varphi} = \omega \boldsymbol{B}\boldsymbol{\varphi}, \tag{3.10}$$

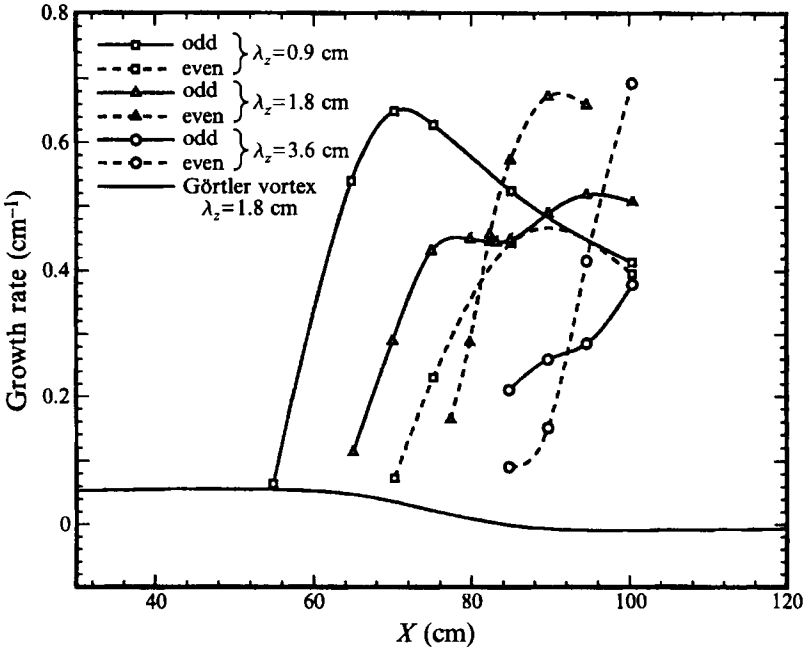

FIGURE 4. Maximum spatial growth rate of the odd and even fundamental modes at various streamwise locations, compared with the growth rate of the Görtler vortex.

Odd mode			Even mode		
X (cm)	f (Hz)	Wavelength (cm)	X (cm)	f (Hz)	Wavelength (cm)
65.0	67.1	4.59	79.8	181.7	1.66
70.0	87.8	3.57	82.3	194.8	1.56
74.9	108.8	2.93	84.9	210.7	1.47
82.3	141.2	2.38	89.7	243.2	1.34
84.9	161.6	2.07	94.6	271.3	1.27
89.7	202.1	1.70	—	—	—
94.6	243.0	1.47	—	—	—

TABLE 1. Frequency and wavelength of the fundamental secondary instability modes, $\lambda_z = 1.8$ cm

where $\boldsymbol{B}$ is a diagonal matrix and $\boldsymbol{A}$ is a square matrix of size $N_y(N_z/2+1)$, where N_y and N_z are the number of collocation points in the y- and z-directions, respectively. This eigenvalue problem is solved by the QR method which yields all the eigenvalues of the discretized system (3.10). Throughout the computations, we use $N_y = 85$ and $N_z = 32$.

The above analysis ignores the effect of viscosity. Yu & Liu (1994), who performed a viscous analysis, noted that the inviscid analysis does not capture the correct eigenfunctions close to the wall. However, here we perform an inviscid analysis since the secondary instability is inflectional and, hence, inviscid in nature and, for the same resolution in the two-dimensional eigenvalue problem, inviscid analysis can be performed with an order-of-magnitude less computer time. Any viscous effects will be accounted for in the PSE analysis we perform in §4 below.

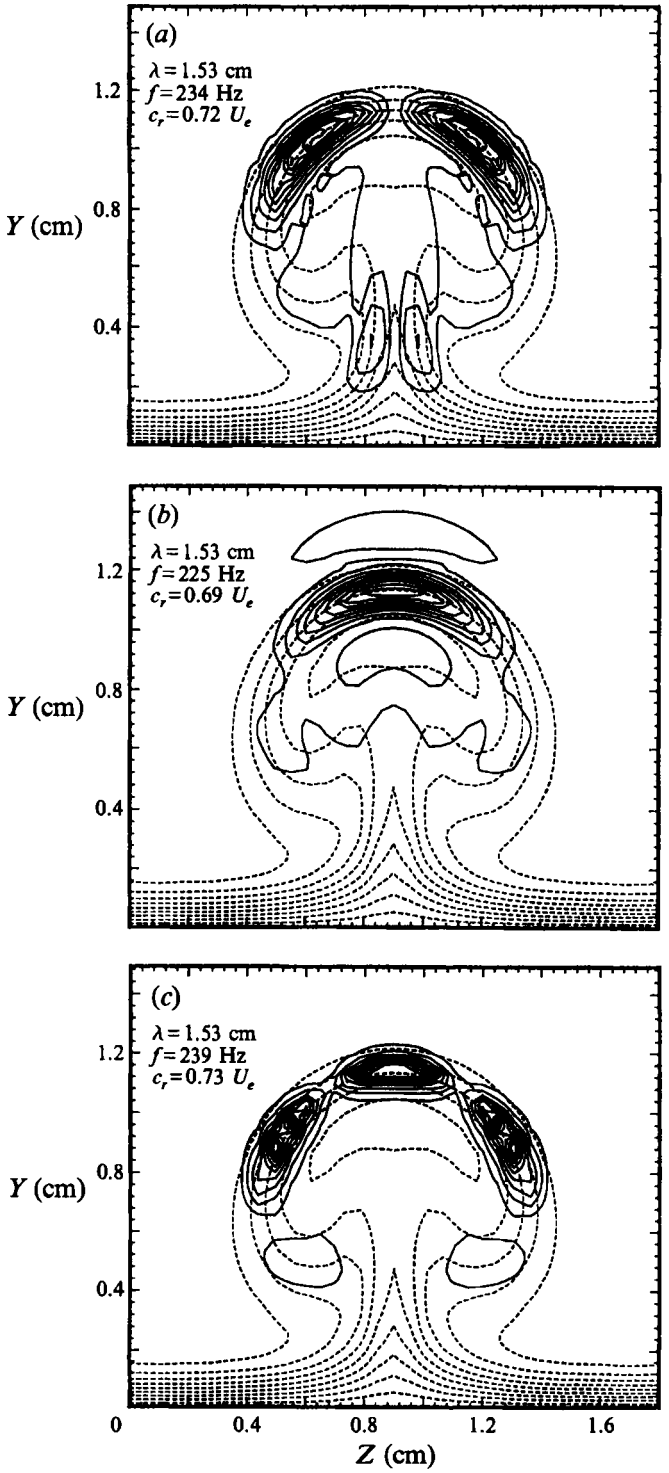

FIGURE 5. Streamwise velocity eigenfunctions (absolute value) of fundamental secondary instability at $X = 95$ cm: (*a*) most unstable odd mode, (*b*) most unstable even mode, (*c*) second most unstable even mode. Dashed lines show the basic flow state.

3.3. *Results of secondary instability calculations*

Secondary instability calculations are carried out for Görtler vortices with wavelengths of 0.9, 1.8 and 3.6 cm. We first present results for the $\lambda_z = 1.8$ cm case for which two-dimensional eigenvalue computations are started at $X = 65$ cm, where the high-frequency oscillations are moderately unstable. Hence, we avoid the difficulty associated with the singularity due to neutral disturbances. The growth rate variation with the streamwise wavenumber at various streamwise locations between $X = 65$ and 100 cm, normalized with scales at $X = 10$ cm, is shown in figure 3(*a*) for odd modes and figure 3(*b*) for even modes. The general trend is that the secondary oscillations become more unstable as the Görtler vortices become stronger downstream. The maximum growth rate at each streamwise location occurs at streamwise wavenumbers approximately between 0.2 and 0.3, corresponding to wavelengths between 1.2 and 1.7 cm. The Blasius boundary-layer thickness in the absence of the Görtler vortices in the range $X = 65$ and 100 cm is approximately between 0.7 and 0.9 cm. This shows that the wavelength of the secondary instabilities is of the order of the boundary-layer thickness. Therefore, our assumption that the basic flow state variation is negligible over the distance of one wavelength is, indeed, justified. We can visually extrapolate the growth rate curves and see that, in this streamwise range, the highest wavenumber where secondary instability occurs is approximately 0.5, corresponding to a wavelength of 0.69 cm.

We now consider the variation of the maximum growth rate of the secondary instabilities with streamwise distance. In order to show that the secondary instability grows much faster than the Görtler vortex, we convert the temporal growth rate to the spatial one by using a group velocity transformation. The use of group velocity to transform temporal growth to spatial growth is well known for primary instabilities (Gaster 1962; Nayfeh & Padhye 1979). Its use for the secondary instability has been addressed by Herbert, Bertolotti & Santos (1985). The value of the group velocity $\partial\omega_r/\partial\alpha$ varies with x and lies in the range 0.6 to 0.72. Figure 4 shows the spatial growth rate of the most unstable even and odd modes for $\lambda_z = 0.9$, 1.8 and 3.6 cm along with the growth rate of the nonlinearly developing Görtler vortex. Since, in the short-wave case ($\lambda_z = 0.9$ cm), the Görtler vortex grows fastest, the odd-mode secondary instability begins to appear at about $X = 50$ cm where the amplitude of the Görtler vortex is about 20%. The even mode becomes unstable further downstream. The odd mode dominates over most of the range $X = 50$ to 100 cm, with the even mode catching up at around $X = 100$ cm. Growth rates of the odd and even modes reach peak values at approximately $X = 70$ and 90 cm, respectively. For the Görtler vortex of medium wavelength ($\lambda_z = 1.8$ cm), the odd mode begins to become significant from approximately $X = 65$ cm and the even mode roughly from $X = 75$ cm, with peak growth rates occurring at $X = 75$ and 95 cm, respectively. An important feature we discover is that, although the odd mode is the first to become unstable, the even mode takes over at roughly $X = 82$ cm to become the most unstable mode. In the long-wave case, the odd mode initially grows faster than the even mode. However, before the odd-mode growth rate becomes significantly large, the even mode begins to dominate. At $X =$ 100 cm, the growth rates of both modes have yet to show signs of reaching peak values. The growth rate of the even mode at $X = 100$ cm is higher than the peak values for the short and medium waves.

We note that the initial dominance of the odd mode over the even mode for the long-wavelength case is weak. Thus, if viscosity had a stabilizing influence on both modes then it is likely that in a viscous calculation, the even mode will become unstable

first. In any case, from the above calculations it is clear that there is a direct influence of the Görtler vortex wavelength on the relative significance of the odd and even modes. For low-wavelength Görtler vortices, the odd mode is strong. The converse appears to be true for the large-wavelength case. For intermediate wavelengths, both modes would have equivalent relevance. In the experiment of SB, the wavelength is around 1.8 cm and both sinuous and varicose modes were observed. There is some experimental evidence that Görtler vortex wavelengths have a direct influence on the type of secondary instability mode. In a related problem (Coriolis-force-induced instability due to rotation) Masuda, Hori & Matubara (1994) found that a horseshoe-type secondary mode appeared for a long-wavelength primary disturbance whereas sinuous secondary motion resulted for short wavelengths of the primary disturbance. Another factor which may have some bearing on the secondary instability mechanism is the Görtler number distribution, which is different in different experiments. However, its influence is believed to be an indirect one through its effect on the development of Görtler vortices and their wavelengths relative to the boundary-layer thickness.

The frequency and wavenumber of the secondary instability corresponding to the maximum growth rate at various streamwise locations are given in table 1 for $\lambda_z =$ 1.8 cm. We see that the frequencies vary greatly from one streamwise station to the next. The experimentally observed frequency of 130 Hz may not be that of the most unstable wave at large downstream distances. The relatively lower-frequency waves (around 100 Hz) become unstable first. When the region of higher-frequency waves is reached, the laminar basic flow state may have already been destroyed by the nonlinear growth of secondary instabilities and the higher-frequency waves may not have a chance to manifest themselves. The temporal direct numerical simulation of Liu & Domaradzki (1993) has a computational box which restricts the maximum wavelength to 2.0 cm. According to table 1, the frequency of most amplified disturbance is about 160 Hz (their calculation gives about 200 Hz). The calculations of Hall & Horseman (1991) were almost exclusively for the basic flow state at $X = 100$ cm. They found that the fastest growing wave (odd mode) has a frequency of about 110 Hz and a wavelength of about 3 cm. This would compare well with our results at about $X =$ 75 cm. This can be explained by noting the fact that the amplitude of their disturbed flow state is apparently lower than ours at corresponding streamwise locations: at $X = 100$ cm, our calculation in figure 2 shows a thin neck while their $\bar{u}(y, z)$ plot does not show this and resembles more the structure computed by us at $X \approx 80$.

We now consider the eigenfunctions of these secondary instability modes at $X =$ 95 cm. The wavelength chosen here is 1.53 cm, close to the fastest growing odd and even modes at this downstream location. In addition to the most unstable odd and even modes, a second even mode is considered. The contours of velocity eigenfunction $|\hat{u}_s|$ at $X = 95$ cm are shown as solid lines in figure 5, together with basic flow state $\bar{u}(y, z)$ as dashed lines in the background. The eigenfunctions are normalized so that the maximum $|\hat{u}_s|$ has an amplitude of unity. The contours plotted are from 0.1 to 0.9 in intervals of 0.1, and $\bar{u}(y, z)$ contours plotted are from 0.1 to 0.9 in intervals of $0.1U_e$. One feature to notice is that the phase speeds, c_r, of the modes shown in figure 5 are all close to $0.7U_e$, and the amplitudes of these modes are concentrated in the neighbourhood of the manifold $\bar{u}(y, z) = 0.7U_e$. This manifold would be the critical layer in the case of neutral stability.

The contours shown in figure 5(*a*) bear some similarity to those obtained by Hall & Horseman (1991) despite the difference between the basic flow states in their work and the present work. The odd mode has two dominant peaks, one on each side of the peak

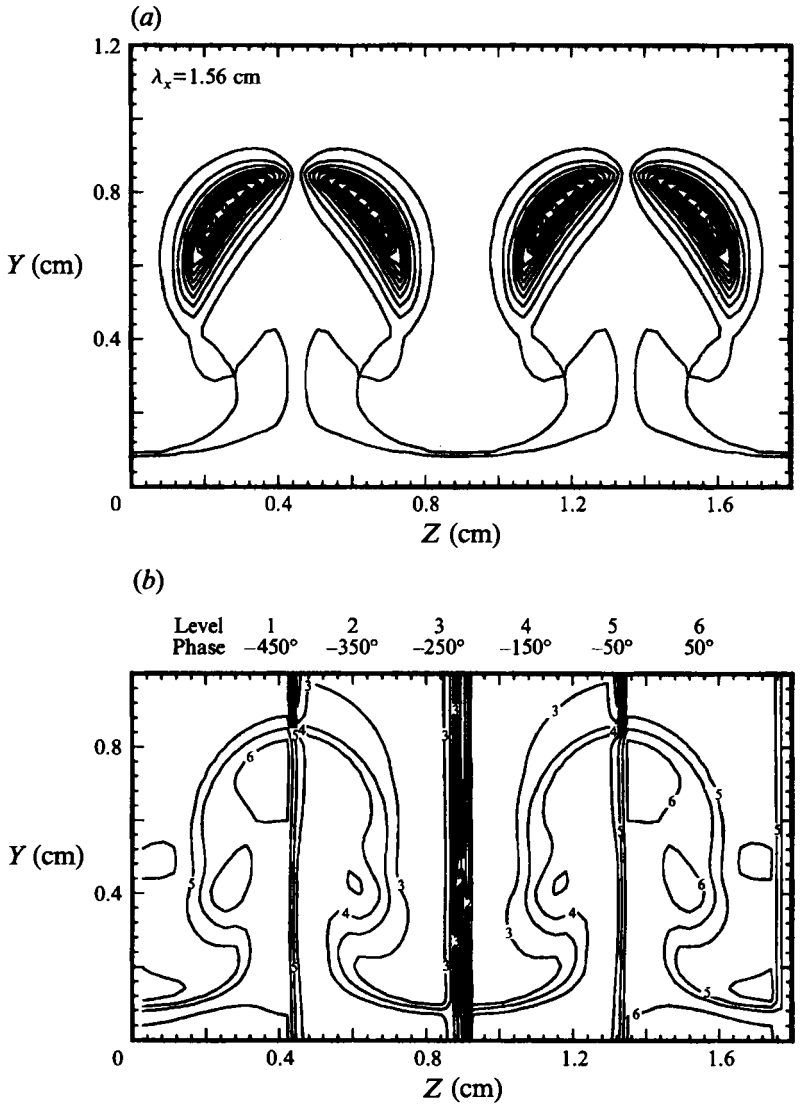

FIGURE 6(*a*). For caption see facing page.

plane. In the case of the even modes, the second even mode (figure 5*c*) has three dominant peaks similar to that shown in figure 6(*a*) of Hall & Horseman (1991) for the only even mode they analysed in their work. The most unstable single-peak even mode was not mentioned in Hall & Horseman (1991). Considering the fact that the growth rate of the first odd mode is about 1.8 times that of the second even mode (see figures 3*a* and 3*b*) and that, in the work of Hall & Horseman (1991), the odd mode grows almost twice as fast as the even mode, we are led to believe that the three-peak even mode analysed by Hall & Horseman (1991) was actually the second unstable even mode, and the first unstable even mode was missed because they used a shooting technique to compute the eigenvalues. In our study, we use a global method which finds all the eigenvalues of the discretized problem.

From the eigenfunctions, we see a definite relationship between instability and inflection in the velocity profiles. The inflection in the velocity profiles occurs at points

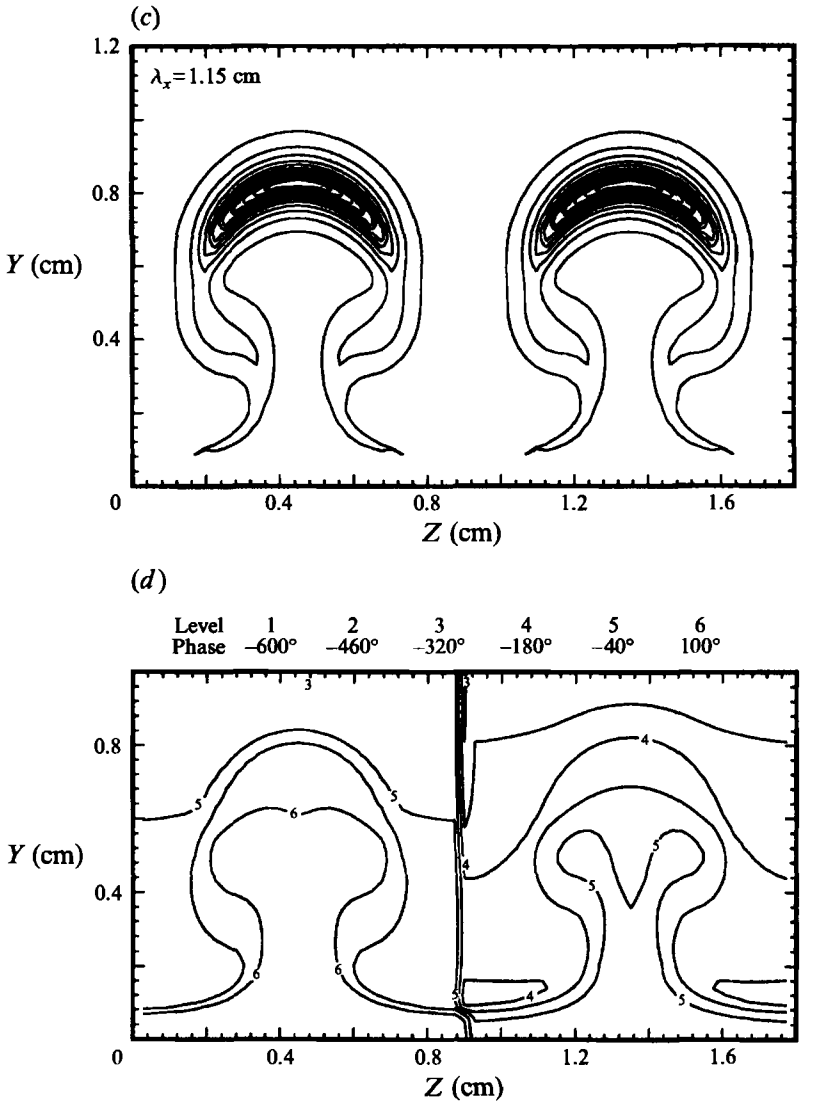

FIGURE 6. Absolute value and phase distribution for the streamwise velocity eigenfunctions for subharmonic secondary instability at $X = 85$ cm: (*a*) odd mode, magnitude, (*b*) odd mode, phase (sinuous), (*c*) even mode, magnitude; (*d*) even mode, phase (varicose).

where the velocity gradient is maximum. Comparisons with vertical ($\bar{u}_y$) and horizontal ($\bar{u}_z$) velocity gradients (not shown) show that the amplitudes of the eigenfunctions concentrate near the regions of maximum velocity gradient. Furthermore, the most unstable even mode appears to be associated with the vertical velocity gradient, the most unstable odd mode with the horizontal velocity gradient and the second most unstable even mode with both gradients.

Finally, we touch upon the subject of subharmonic instability. The sinuous and varicose modes we have discussed so far and those studied by Hall & Horseman (1991) and Yu & Liu (1991, 1994) have spanwise wavelengths equal to those of the primary Görtler vortices. They are the fundamental modes. Each mushroom structure formed by a pair of counter-rotating Görtler vortices, when subject to these disturbances,

	Frequency (Hz)	Streamwise wavelength (cm)	Growth rate (s^{-1})
Fundamental (s)	253	1.41	187
Subharmonic (s)	233	1.63	107
Fundamental (v)	275	1.27	152
Subharmonic (v)	303	1.13	152

TABLE 2. Comparison of most unstable fundamental and subharmonic modes at $X = 85$ cm, $\lambda_z = 0.9$ cm (s = sinuous, v = varicose)

moves synchronously with adjacent mushrooms. It is also possible for a pair of adjacent mushrooms to swing in opposite directions. In fact, a close examination of the results of SB shows such oscillations (e.g. see the middle two streaks in figure 14*c* of SB). It is clear that these oscillations cannot originate from fundamental secondary instability modes, but can be attributed to the subharmonic instability modes having spanwise wavelengths equal to twice those of the primary Görtler vortices. For Görtler vortices with large wavelengths, the mushrooms are separated by wide valley regions as indicated by the nonlinear development of Görtler vortices of wavelengths 3.6 cm (figure 2). In this case the mushroom may tend to swing on its own without much interaction with its neighbours. On the other hand, for small wavelengths, the presence of the adjacent mushrooms is noticed. Therefore, the subharmonic mode of secondary instability may be pronounced for the low-wavelength case and, therefore, we choose $\lambda_z = 0.9$ cm to do the subharmonic analysis.

In the framework of the present two-dimensional eigenvalue problem, we include two periods of Görtler vortices in the basic flow $\bar{u}$ to use in (3.3)–(3.6). Computations are carried out at $X = 85$ cm. It is found that both fundamental sinuous and varicose modes have their respective subharmonic counterparts. The eigenfunctions (magnitude and phase) of the subharmonic modes are given in figure 6. These look very similar to those of the fundamental modes, except that each subharmonic mode goes through a phase change of 180° from one mushroom to the next. Hence, owing to the subharmonic instability, there are regions where the two mushrooms are attracted to each other while in other regions they move apart. Table 2 lists the frequency, wavelength and growth rate of the most unstable subharmonic modes at $X = 85$ cm together with their fundamental counterparts. It can be seen that, in this case, the subharmonic modes are significant. The growth rate of the subharmonic sinuous mode is over half that of the fundamental sinuous mode. The subharmonic varicose mode grows as fast as the fundamental varicose mode. These results imply that the subharmonic modes are as likely to appear as the fundamental modes. The sinuous subharmonic mode gives rise to anti-phase swings of the mushroom structures, leading to the swallowing of one mushroom by another. In the subharmonic varicose mode, the horseshoe vortex structures are simply shifted in the streamwise direction with respect to the adjacent mushrooms.

4. Nonlinear development of unsteady disturbances

We now solve (2.7)–(2.8) to study nonlinear evolution of the steady and unsteady disturbances. Calculations are performed for fundamental mode only and for $\lambda_z = 1.8$ cm. The spatial secondary instability computations for the even and odd modes are started at streamwise locations where the respective modes are moderately unstable.

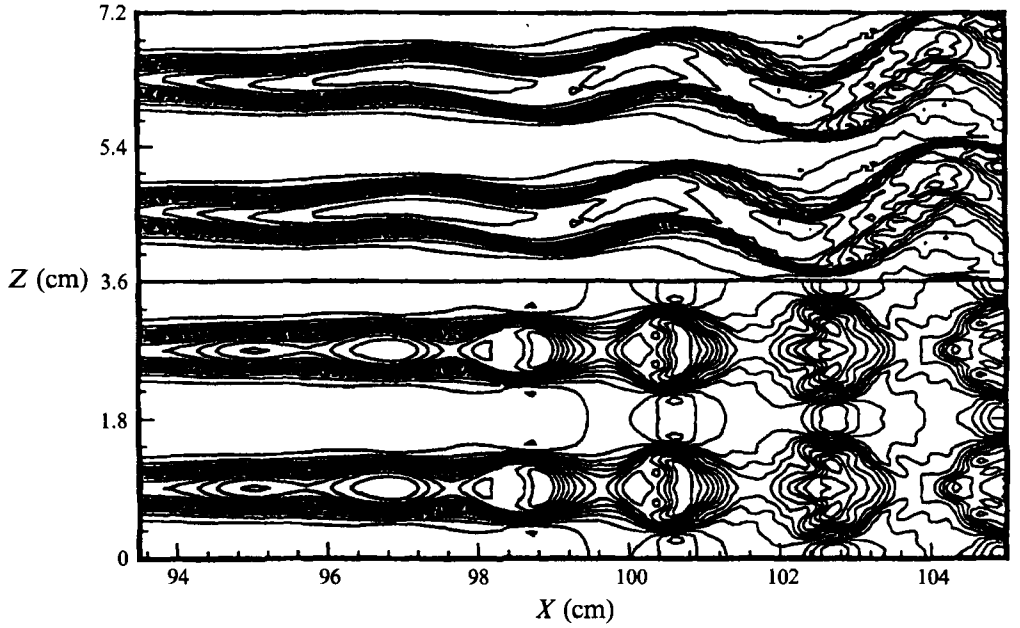

FIGURE 7. Instantaneous streamwise velocity in the (X, Z)-plane at $Y = 1.08$ cm: top – sinuous mode (odd), (bottom) – varicose mode (even).

Since exact initial conditions are difficult to obtain, we use the eigenfunctions obtained from inviscid linear secondary instability analysis to approximate these conditions. Calculations show that transients decay very fast. The initial amplitude assigned to these disturbances is small enough (of $O(10^{-5})$ in $\hat{u}_s$ for both odd and even modes) to ensure that the initial evolution of the secondary instability is linear.

We first plot the instantaneous streamwise velocity contours in the (x, z)-plane at $Y = 1.08$ cm (figure 7). We see that the odd mode perturbs the Görtler vortices in a wavy (or sinuous) manner, while the even mode breaks up the otherwise straight contours of Görtler vortices into series of knotty structures associated with the horseshoe vortex mode of break down. At large downstream distances, more and more small-scale structures begin to appear, as the flow heads for transition to turbulence. The structure of the subharmonic odd mode would bring the two mushrooms closer in some regions and further apart in others. As noted above, the structure of the subharmonic even mode will be similar to that shown in figure 7 for the fundamental mode except that the adjacent knots will be approximately 180° out of phase.

Now we discuss the detailed results for the odd mode. These calculations are performed in the following way. We start the calculations at $X = 10$ cm for the steady disturbances only. These calculations are carried out up to $X = 75$ cm where the unsteady odd-mode disturbances are introduced. The frequency of the fundamental secondary instability is chosen to be 110 Hz, very close to the most unstable odd mode at that location (109 Hz). The number of Fourier modes is 11 in the spanwise direction ($-10 \leqslant n \leqslant 10$) and 8 in time ($-7 \leqslant m \leqslant 7$). Figure 8 shows contours of streamwise r.m.s. fluctuations at four streamwise locations downstream of the starting location. Initially, the shape of the amplitude distribution closely resembles the local eigenfunctions analysed in the last section, except for some differences near the wall (e.g. compare figures 5*a* and 8*b*). These differences may be attributed to viscous effects. Later on, at larger X, nonlinearity causes the amplitude distribution to become fatter,

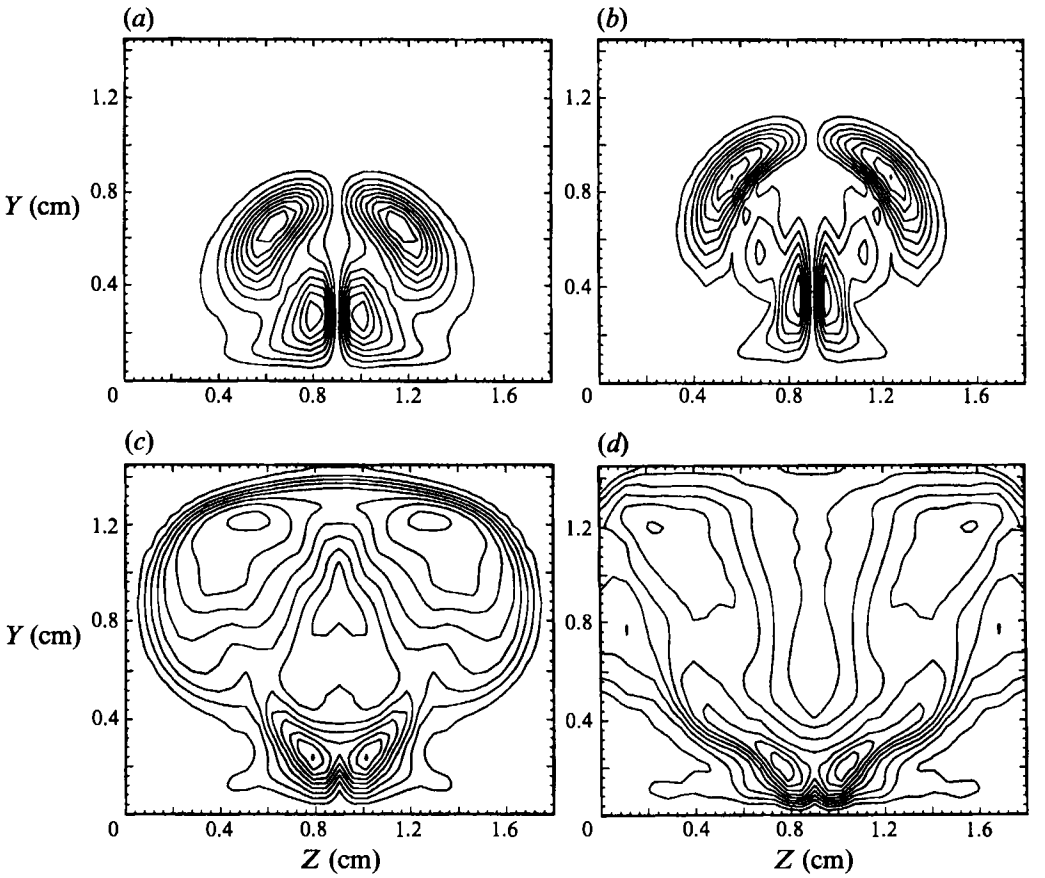

FIGURE 8. Variation of r.m.s. streamwise velocity fluctuations in the (Y, Z)-plant at $f = 110$ Hz for the fundamental odd mode: (*a*) $X = 80.4$ cm, the outermost contour value = 0.00001 with an increment of 0.000001; (*b*) $X = 91.3$ cm, outer contour value = 0.002 with an increment of 0.002; (*c*) $X = 102.3$ cm, contours (0.02, 0.02); (*d*) $X = 105$ cm, contours (0.02, 0.02).

beginning to fill up the (Y, Z)-plane. The maximum amplitude reaches about 20% of the free-stream velocity U_e. There are two regions of high amplitude: one near the wall and the other away from the wall. Initially the region near the boundary-layer edge has higher amplitude, but as the disturbances evolve downstream the near-wall region attains higher amplitude. The contours of $\hat{u}_{rms}$ for the odd mode are similar to the streamwise r.m.s. fluctuations shown in figure 15 of the temporal simulation of Liu & Domaradzki (1993), suggesting that this mode indeed plays an important role in the break-up of Görtler vortices.

The contours of streamwise mean flow (time-averaged flow) at $X = 102.3$ cm are shown in figure 9. The changes in the mushroom structure from that without the high-frequency oscillations are profound (compare with figure 2*b*). The top of the mushroom becomes flatter because strong unsteady oscillations smear out the differences in velocity gradients. As the oscillations get stronger, the thin neck region of the mushroom, where low-speed fluid lifts up, becomes confined to the neighbourhood close to the wall. The experiments of SB show similar structure of the vortices prior to break down, except that in their experiment vortices tend to lose symmetry about the peak plane. Some of our calculations suggest that such loss of

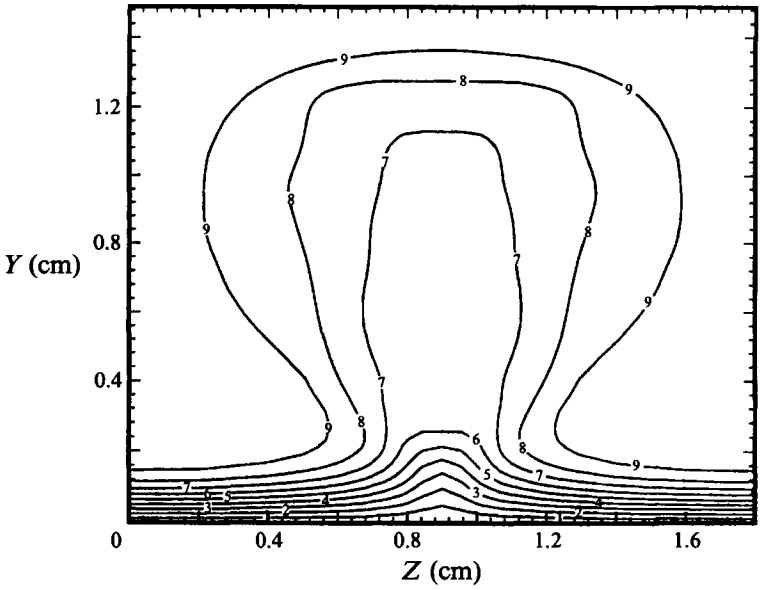

FIGURE 9. Variation of time-averaged streamwise velocity in the (Y, Z)-plane at $X = 102.3$ cm; fundamental odd mode. Contour values range from 0.1 in increments of 0.1.

symmetry is linked to the unsymmetric initial disturbance field. We also note that the computed isocontours of streamwise velocity for the odd mode at $X = 102.3$ cm shown in figure 9 agree much better with results of SB at 110 cm than at 100 cm.

We now present computations for the even mode, which is introduced at the streamwise location $X = 82$ cm. The frequency of the fundamental secondary instability is taken to be 195 Hz, which is the frequency of the most unstable even mode at that location. The number of Fourier modes is the same as in the odd-mode case. The r.m.s. values of streamwise fluctuations are shown in figure 10. In the early linear stage, the distribution of amplitude of the streamwise r.m.s. fluctuation is concentrated in the region away from the wall, as in the results shown in figure 5(*b*). Nonlinear interaction increases the perturbation level near the wall.

In their numerical simulation, Liu & Domaradski (1993) observed that the oscillation frequency of the vertical velocity is twice that of the spanwise velocity in the low-speed region, while the two frequencies are the same away from that region. This is also found to be the case in the present computations for the odd mode. Figure 11 shows the vertical and spanwise velocity fluctuations at two fixed locations in space, one in the low-speed region, the other away from it. Counting the number of dominant peaks, we can observe the difference in frequency in the low-speed region. This phenomenon can be explained by considering the spatial-symmetry-preservation property of the fundamental secondary instability and its harmonics. Initially, the only mode present is the fundamental with frequency, say, f. In the odd-mode case, the vertical velocity fluctuation for the fundamental mode is odd with respect to the line of symmetry of the background mushroom structure, while the spanwise velocity fluctuation is even. It can be mathematically verified that the symmetry properties of the harmonics obey the following rule: for the vertical velocity, modes with frequencies $2f$, $4f$, $6f$, etc. are even, while modes with frequencies $3f$, $5f$, $7f$, etc. are odd; for the spanwise velocity, modes with frequencies $2f$, $4f$, $6f$, etc. are odd, while modes with frequencies $3f$, $5f$, $7f$, etc. are even. These symmetry properties are preserved as the flow

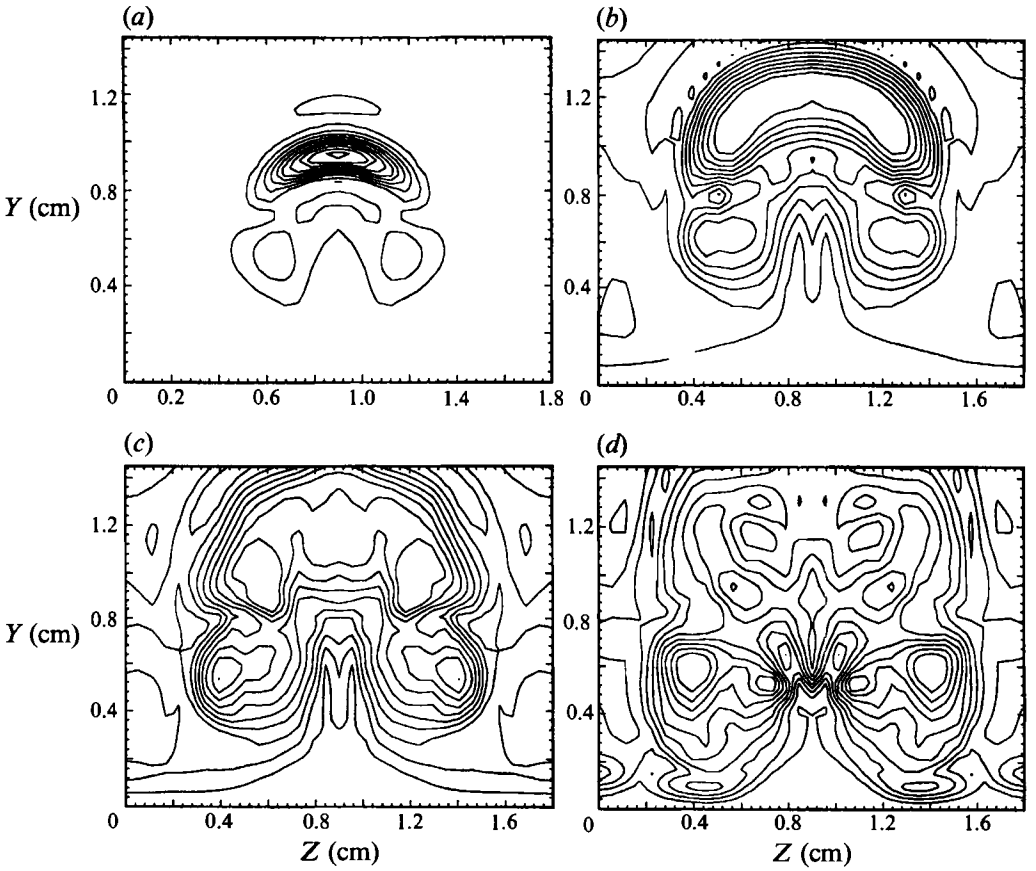

FIGURE 10. Variation of r.m.s. streamwise velocity fluctuations in the (Y, Z)-plane at $f = 195$ Hz for the fundamental even mode: (*a*) $X = 87.8$ cm, the outermose contour value = 0.00002 with an increment of 0.00002; (*b*) $X = 100.4$ cm, contours (0.01, 0.01); (*c*) $X = 102.3$ cm, contours (0.01, 0.01); (*d*) $X = 106.7$ cm, contours (0.01, 0.01).

develops downstream. Suppose we place a velocity probe somewhere along the line of symmetry of the background mushroom structure; we cannot detect the amplitude of the fundamental mode of the vertical velocity since it is odd and, therefore, has zero-amplitude there. The lowest-frequency mode that can be detected is the $2f$ mode of the vertical velocity. The lowest-frequency mode of the spanwise velocity that can be detected is the fundamental mode. Hence, it appears that, in the peak region, the frequency of the vertical velocity is twice that of the spanwise velocity. Once we move away from the peak region, the fundamental modes of both the vertical and the spanwise velocities can be detected; therefore, the same frequencies are observed.

5. Conclusions

Linear secondary instability analysis for Görtler vortices is carried out using a two-dimensional eigenvalue approach. For the conditions of the experiment of SB ($\lambda_z = 1.8$ cm), the odd mode of secondary instability begins to appear at approximately $X = 60$ cm, the even mode becomes unstable later at approximately $70 < X < 75$ cm. At about $X = 82$ cm, the even mode becomes more unstable than the odd mode. Comparisons of the amplitude distributions of eigenfunctions with the distributions of

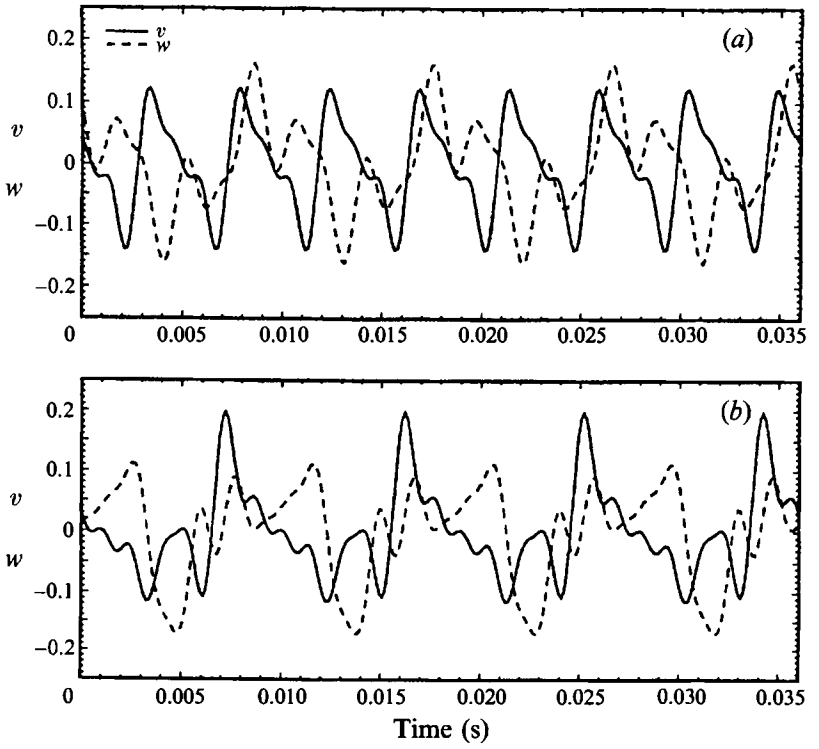

FIGURE 11. Vertical and spanwise velocity fluctuations with time at $X = 105$ cm and $Y = 1.29$ cm: (*a*) fluctuations at the peak, (*b*) fluctuations at $Z = \lambda_z/4$ away from the peak.

vertical and spanwise shear gradients indicates the close association of the most unstable even mode with the vertical shear and the most unstable odd mode with the spanwise shear.

It is shown that the relative significance of the odd and even modes depends upon the Görtler vortex wavelength. Thus the short-wavelength vortices show a stronger tendency towards the odd modes and the long-wavelength vortices towards the even modes. This result is supported by experiments.

The above work as well as previous investigations (Hall & Horseman 1991; Yu & Liu 1991, 1994) have addressed fundamental modes of secondary instability. In this paper, we also investigate subharmonic instability by extending the spanwise computational domain to twice the wavelength of the Görtler vortex. We find that both the even and odd modes have corresponding subharmonics with growth rates comparable to those for the fundamental modes. It is likely that subharmonic modes are more relevant for short-wavelength Görtler vortices.

The nonlinear spatial development of the odd and even modes of secondary instability is computed using the PSE method. The odd and even modes give rise to the sinuous instability and the varicose instability, respectively. Prior to break down to turbulence, the nonlinear interaction among the steady and unsteady modes eventually makes the Görtler vortices oscillate sinuously in the plane parallel to the plate or causes them to develop horseshoe-type structures which travel downstream. Both modes of break down have been found in the experiment. The two-fold difference between the frequency of the vertical velocity and that of the spanwise velocity oscillations found by Liu & Domaradzki (1993) is simply due to the fundamental mode of the vertical

velocity having zero amplitude at the line of symmetry of the mushroom for the sinuous instability, and the high frequency in the vertical velocity that they detected was, in fact, for the harmonic.

This work was sponsored under AFOSR contract F49620-91-C-0014 with Dr James M. McMichael as the technical monitor. The authors are indebted to one of the referees who pointed out an error in an earlier version of the manuscript.

Appendix

Let

$$\Delta = -\mathrm{i}m\omega + \mathrm{i}\alpha_{mn} U + \frac{\alpha_{mn}^2}{R} - \frac{\mathrm{i}}{R}\frac{\mathrm{d}\alpha_{mn}}{\mathrm{d}x},$$

then

$$\boldsymbol{L}_0 = \begin{bmatrix} \Delta + \dfrac{\partial U}{\partial x} + \kappa V & \dfrac{\partial U}{\partial y} + \kappa U & 0 & \mathrm{i}\alpha_{mn} \\ \dfrac{\partial V}{\partial x} - 2\kappa U & \Delta + \dfrac{\partial V}{\partial y} & 0 & 0 \\ 0 & 0 & \Delta & \mathrm{i}n\beta \\ \mathrm{i}\alpha_{mn} & \kappa & \mathrm{i}n\beta & 0 \end{bmatrix},$$

$$\boldsymbol{L}_1 = \begin{bmatrix} V - \dfrac{\kappa}{R} & 0 & 0 & 0 \\ 0 & V - \dfrac{\kappa}{R} & 0 & 1 \\ 0 & 0 & V - \dfrac{\kappa}{R} & 0 \\ 0 & 1 & 0 & 0 \end{bmatrix},$$

$$\boldsymbol{L}_2 = \begin{bmatrix} -\dfrac{1}{R} & 0 & 0 & 0 \\ 0 & -\dfrac{1}{R} & 0 & 0 \\ 0 & 0 & -\dfrac{1}{R} & 0 \\ 0 & 0 & 0 & 0 \end{bmatrix},$$

$$\boldsymbol{L}_3 = \begin{bmatrix} U - \dfrac{2\mathrm{i}\alpha_{mn}}{R} & 0 & 0 & 1 \\ 0 & U - \dfrac{2\mathrm{i}\alpha_{mn}}{R} & 0 & 0 \\ 0 & 0 & U - \dfrac{2\mathrm{i}\alpha_{mn}}{R} & 0 \\ 1 & 0 & 0 & 0 \end{bmatrix}.$$

$\boldsymbol{N}_{mn}$ is the Fourier transform of $(N_1, N_2, N_3, 0)^T$ in (2.1)–(2.4).

REFERENCES

AIHARA, Y. & KOYAMA, H. 1981 Secondary instability of Görtler vortices: formation of periodic three-dimensional coherent structures. *Trans. Japan Soc. Aero. Space Sci.* **24**, 78–94.

BECKWITH, I. E., MALIK, M. R., CHEN, F.-J. & BUSHNELL, D. M. 1984 Effects of nozzle design parameters on the extent of quiet test flow at Mach 3.5. *IUTAM Symp. on Laminar–Turbulent Transition, Novosibirsk, USSR* (ed. V. V. Kozlov), pp. 589–600.

BERTOLOTTI, F. P., HERBERT, TH. & SPALART, P. R. 1992 Linear and nonlinear stability of the Blasius boundary layer. *J. Fluid Mech.* **242**, 441–474.

BIPPES, H. 1978 Experimental study of the laminar–turbulent transition of a concave wall in a parallel flow. *NASA TM*-75243.

CHANG, C.-L., MALIK, M. R., ERLEBACHER, G. & HUSSAINI, M. Y. 1991 Compressible stability of growing boundary layers using parabolized stability equations. *AIAA Paper* 91-1636.

FLORYAN, J. M. 1991 On the Görtler vortex instability of boundary layers. *Prog. Aerospace Sci.* **28**, 235–271.

GASTER, M. 1962 A note on the relation between temporarlly increasing and spatially increasing disturbances in hydrodynamic stability. *J. Fluid Mech.* **14**, 222–224.

GUO, Y. & FINLAY, W. H. 1994 Wavenumber selection and irregularity of spatially developing nonlinear Dean and Görtler vortices. *J. Fluid Mech.* **264**, 1–40.

HALL, P. 1983 The linear development of Görtler vortices in growing boundary layers. *J. Fluid Mech.* **30**, 41–58.

HALL, P. 1988 The nonlinear development of Görtler vortices in growing boundary layers. *J. Fluid Mech.* **193**, 243–266.

HALL, P. 1990 Görtler vortices in growing boundary layers: the leading edge receptivity problem, linear growth, and nonlinear breakdown stage. *Mathematika* **37**, 151–189.

HALL, P. & HORSEMAN, N. J. 1991 The linear inviscid secondary instability of longitudinal vortex structures in boundary layers. *J. Fluid Mech.* **232**, 357–375.

HALL, P. & LAKIN, W. D. 1988 The fully nonlinear development of Görtler vortices in growing boundary layers. *Proc. R. Soc. Lond.* A **415**, 421–444.

HERBERT, TH. 1991 Boundary-layer transition – analysis and prediction revisited. *AIAA Paper* 91-0737.

HERBERT, TH., BERTOLOTTI, F. P. & SANTOS, G. R. 1985 Floquet analysis of secondary instability in shear flows. In *Stability of Time Dependent and Spatially Varying Flows* (ed. D. L. Dwoyer & M. Y. Hussaini), pp. 48–57. Springer.

HUERRE, P. & MONKEWITZ, P. A. 1990 Local and global instabilities in spatially developing flows. *Ann. Rev. Fluid Mech.* **22**, 473–537.

ITO, A. 1985 Breakdown structure of longitudinal vortices along a concave wall. *J. Japan Soc. Aero. Space Sci.* **33**, 116–173.

LEE, K. & LIU, J. T. C. 1992 On the growth of mushroomlike structure in nonlinear spatially developing Görtler vortex flow. *Phys. Fluids* A **4**, 95–103.

LIU, W. & DOMARADZKI, J. A. 1993 Direct numerical simulation of transition to turbulence in Görtler flow. *J. Fluid Mech.* **246**, 267–299.

MALIK, M. R., CHUANG, S. & HUSSAINI, M. Y. 1982 Accurate numerical solution of compressible stability equations. *Z. Angew. Math. Phys.* **33**, 189–201.

MALIK, M. R. & LI, F. 1992 Three-dimensional boundary layer stability and transition. *SAE Paper No.* 921991. Presented at SAE Aerotech '92, Anaheim, CA.

MALIK, M. R. & LI, F. 1993 Secondary instability of Görtler and crossflow vortices. In *Proc. Int. Symp. on Aerospace and Fluid Science*, pp. 460–477. Institute of Fluid Science, Tohoku University, Sendai, Japan.

MALIK, M. R., LI, F. & CHANG, C.-L. 1994 Crossflow disturbances in three-dimensional boundary layers: nonlinear development, wave interaction and secondary instability. *J. Fluid Mech.* **268**, 1–36.

MASUDA, S., HORI, D. & MATUBARA, M. 1994 Secondary instability associated with streamwise vortices in a rotating boundary layer. *IUTAM Symp. on Laminar-Turbulent Transition, Sendai, Japan* (to appear).

NAYFEH, A. H. & PADHYE, A. 1979 The relation between temporal and spatial stability in three-dimensional flows. *AIAA J.* **17**, 1084–1090.

PEERHOSSAINI, H. & WESFREID, J. E. 1988 On the inner structure of streamwise Görtler rolls. *Intl J. Heat Fluid Flow* **9**, 12–18.

SABRY, A. S. & LIU, J. T. C. 1991 Longitudinal vorticity elments in boundary layers: nonlinear development from initial Görtler vortices as a prototype problem. *J. Fluid Mech.* **231**, 615–663.

SARIC, W. S. 1994 Görtler vortices. *Ann. Rev. Fluid Mech.* **26**, 379–409.

SWEARINGEN, J. D. & BLACKWELDER, R. F. 1987 The growth and breakdown of streamwise vortices in the presence of a wall. *J. Fluid Mech.* **182**, 255–290 (referred to herein as SB).

YU, X. & LIU, J. T. C. 1991 The secondary instability in Görtler flow. *Phys. Fluids* A **4**, 1825–1827.

YU, X. & LIU, J. T. C. 1994 On the mechanism of sinuous and varicose modes in three-dimensional viscous secondary instability of nonlinear Görtler rolls. *Phys. Fluids* **6**, 736–750.